

Electrostatically driven vacuum-encapsulated polysilicon resonators

Part II. Theory and performance

Harrie A.C. Tilmans*, Rob Legtenberg

MESA Research Institute, University of Twente, PO Box 217, 7500 AE Enschede, Netherlands

Received 1 July 1993; accepted in revised form 2 June 1994

Abstract

In this paper, the design, modelling and performance characteristics of electrostatically driven vacuum-encapsulated polysilicon resonators are addressed. A one-port configuration is preferably employed for excitation and detection of the vibration. Mechanical instability (pull-in) is discussed on the basis of the energy minimum principle. An expression for the pull-in voltage of a beam is given. The electromechanical behaviour in a limited frequency regime around the fundamental resonance is accurately modelled by an electric circuit consisting of a (static) capacitor shunted by a series (dynamic) *RLC* branch. The d.c. bias dependence of the circuit components and of the series resonance frequency has been experimentally investigated and is compared with the theory. The large-amplitude behaviour is discussed as well. The plate modulus and residual strain of boron-doped polysilicon are estimated from the resonance frequencies of microbridges of varying lengths. The feasibility of their application as resonant strain gauges is investigated. The 210 μm long beams typically have an unloaded fundamental frequency of 324 kHz, a gauge factor of 2400 and an uncompensated temperature coefficient of $\sim 135 \text{ ppm } ^\circ\text{C}^{-1}$.

Keywords: Electrostatic excitation and detection; Polysilicon resonators; Vacuum encapsulation; Equivalent circuit; Pull-in; Hard spring effect

1. Introduction

In the field of mechanical sensors, resonant sensors have proved to offer the highest resolution, performance and long-term stability at present [1–6]. They have traditionally been used in high-precision applications. The main feature of a resonant sensor is its frequency (shift) output, which is readily converted into a digital output signal. The central part of the sensor is a vibrating mechanical element called the resonator, which provides the frequency shift output. In order to eliminate resonance frequency shifts due to physical (e.g., mass loading, dust, vapour adsorption) and chemical (e.g., corrosion) interactions of the resonator with the surroundings and, further, to attain a high mechanical quality factor, the resonator must be housed in an evacuated cavity. Recent work on local sealing, whereby the resonator is placed inside an evacuated microcavity,

defines a novel trend in the future development of resonant mechanical sensors [4,7–13]. The resonator together with the surrounding shell can be considered as a resonant strain gauge, which replaces the more conventional piezoresistance strain gauge.

In this paper, the design, theory and performance characteristics of vacuum-encapsulated polysilicon resonating beams are described. The resonators are preferably operated in a one-port configuration based on electrostatic drive and detection mechanisms [14–19]. As opposed to earlier designs [3–10], this scheme does not suffer from disturbing frequency shifts due to thermally induced axial loads, it can be represented by a very simple equivalent circuit, it leads to a homogeneous resonator, thus eliminating built-in static moments, and to a minimum number of interconnecting wires (i.e., two) along with a rather simple layout structure. This paper forms Part II of a set of two papers dealing with electrostatically driven vacuum-encapsulated polysilicon resonators. Here, theory and performance issues are

*Present address: Katholieke Universiteit Leuven, Departement Elektrotechniek-ESAT, Kardinaal Mercierlaan 94, B-3001 Heverlee, Belgium.

mainly addressed, whereas Part I [20] focuses upon details of the fabrication process.

2. Design and fabrication

2.1. Design

A cross section of the basic structure of the resonator is shown schematically in Fig. 1. The resonator consists of a prismatic beam with a rectangular cross section and is housed in an evacuated cavity. Electrostatic excitation and detection is employed [14-19]. From an electric viewpoint, the structure defines a four-terminal device. Both the one- [16,18,19] and two-port [7,9,14, 15,17] approaches can be used for excitation and detection, as indicated by the driving schemes of Table 1. In the one-port configuration either one of the two air-gap capacitors, as depicted in Fig. 1, can be used. In this configuration, a d.c. polarization voltage V_p and an a.c. drive voltage $v(t)$ are superimposed and applied to the resonator, while the other capacitor plate is grounded. In a two-port configuration, the resonator will be connected to the d.c. polarization voltage. Either the substrate or the cap can be used as the respective excitation or detection electrode. At the excitation site, an a.c. drive voltage is applied, while at the detection site an a.c. current is measured. It turned out that resonators configured as a one-port according to scheme Ia (see Table 1) gave the best results in terms of a

high signal-to-noise ratio and a small influence of parasitic loads.

2.2. Fabrication

Surface micromachining was used for fabrication. The resonators are 210-510 μm long, 100 μm wide and 1.5 μm thick, with a gap spacing of approximately 1.2 μm . The thickness of the sealing cap is approximately 2.6 μm . Fine-grained polysilicon grown by low-pressure chemical vapour deposition (LPCVD) was used as a structural material and undoped plasma-enhanced chemical vapour deposition (PECVD) oxides were used as the sacrificial-layer materials. The conducting areas of the capacitor plates were defined by (local) boron implantation of the silicon substrate, the polysilicon beam and the cap. The electrodes are mutually insulated through thin LPCVD silicon nitride layers. Following removal of the sacrificial layers in HF and appropriate rinsing, freeze drying from cyclohexane was used to prevent sticking of the beams to the substrate (or to the cap). Evacuation of the cavity was achieved through reactive sealing with LPCVD silicon nitride. It is noted that the sealing material must have good insulating properties, otherwise the electric terminals labelled 1, 2 and 3 in Fig. 1 will be short circuited. An SEM photograph of a sealed polysilicon resonator is shown in Fig. 2. Details of fabrication are presented in the accompanying paper [20].

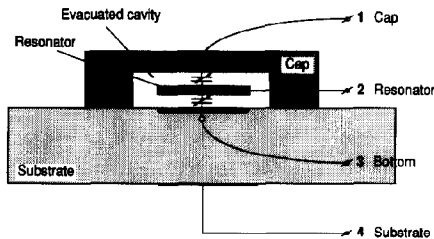


Fig. 1. Schematic cross section of a vacuum-encapsulated flexural beam resonator depicted as a four-terminal device.

Table 1

Electrical driving schemes, indicating the terminal voltages of the structure depicted in Fig. 1, for both one-port and two-port configurations. The 'null' indicates the low-voltage terminal of the impedance measurement system and 'gnd' stands for ground potential. Further, V_p indicates the d.c. polarization voltage and $v(t)$ the a.c. driving voltage

Terminal	One-port				Two-port	
	Ia	Ib	Ic	Id	IIa	IIb
1	$V_p + v(t)$	null	null	$V_p + v(t)$	gnd	$v(t)$
2	$V_p + v(t)$	$V_p + v(t)$	null	null	V_p	V_p
3	null	$V_p + v(t)$	$V_p + v(t)$	null	$v(t)$	gnd
4	gnd	$V_p + v(t)$	$V_p + v(t)$	gnd	$v(t)$	gnd

3. Theory of the electrostatic one-port resonator

A theoretical model is derived for resonators configured as one-port according to one of the schemes



Fig. 2. SEM photograph of a sealed polysilicon resonator, 410 μm long, 100 μm wide and 1.5 μm thick. The three bonding pads for electrical connection with the cap (upper), the bottom (lower) and the beam (right) are clearly visible.

Ia, Ib, Ic or Id of Table 1. The resonator is assumed to be a beam that is initially flat, prismatic, homogeneous and wide (i.e., $b > 5h$, where b is the beam width and h the beam thickness). A sketch of the resonator configured as a one-port type is shown in Fig. 3. The resonant beam is composed of a conducting material and defines the upper electrode. The lower electrode is stationary, has a rectangular shape and is concentric with the beam surface. It is noted, that, although the theory is developed for a one-port resonator, most of the results are directly applicable to two-port resonators as well.

3.1. Static behaviour and 'pull-in'

A d.c. polarization voltage causes an attractive electrostatic force between the capacitor electrodes that is inversely proportional to the square of the gap spacing. This makes the force dependent on the deflection, leading to non-linear behaviour. For a beam subjected to a (tensile) axial force N , the static deflection profile $w^0(x)$ is governed by the following non-linear differential equation of equilibrium:

$$\hat{E}I \frac{d^4 w^0(x)}{dx^4} - N \frac{d^2 w^0(x)}{dx^2} = q_0(w^0(x), V_P)$$

$$= \frac{1}{2} \frac{\epsilon_0 V_P^2}{[d - w^0(x)]^2} \int_b S(w, y) dy \quad (1)$$

where $\hat{E} = E/(1 - \nu^2)$ is the plate modulus, and E and ν are Young's modulus and Poisson's ratio of the beam material, respectively, I is the second moment of inertia of the beam cross section, $q_0(w^0(x), V_P)$ denotes the static electrostatic force per unit beam length as a function of position x and the d.c. polarization voltage V_P , d is the zero-voltage gap spacing, ϵ_0 is the dielectric constant of vacuum, $S(x, y)$ is the spatial distribution function describing the active electrode area, i.e., the

electrode overlap, and the integral limit b indicates that the integral must be evaluated over the entire beam width. To eliminate torsional deformations, the electrode overlap function $S(x, y)$ is limited to symmetric patterns with respect to the x -axis. This allows one-dimensional modelling of the beam behaviour. An analytical closed-form solution of the above equation cannot be found and approximate methods have to be used. This can be done in several ways. One way is to solve the differential equation numerically based on an iterative process. Details of this procedure have been published elsewhere [19]. Other methods are based on the principle of stationary potential energy, also known as the energy minimum principle [21]. The Rayleigh–Ritz method is such a method. An approximate solution $\tilde{w}^0(x)$ to the differential Eq. (1) is constructed in the form of a linear combination of admissible trial functions:

$$\tilde{w}^0(x) = \sum_{i=1}^n a_i g_i(x) \quad (2)$$

where a_i are coefficients to be determined and $g_i(x)$ are admissible trial functions. The principle of stationary potential energy selects the a_i of the assumed displacement field so as to superpose various trial functions in a way that most nearly satisfies the differential equation of equilibrium. The trial functions can be polynomials, mode shape functions, trigonometric functions, etc. The next step is to derive the total potential energy and render it stationary in order to obtain the equilibrium position. If the non-linear energy term due to large deflections is ignored, the total potential energy, denoted by Π , can be expressed as

$$\Pi = \Pi(a_1, a_2, \dots, a_n) = U_b + U_m + V_{el} \quad (3)$$

where U_b and U_m are the strain energy terms due to bending and to membrane stretching, respectively, and V_{el} denotes the potential energy of the electrostatic force $q_0(x, V_P)$:

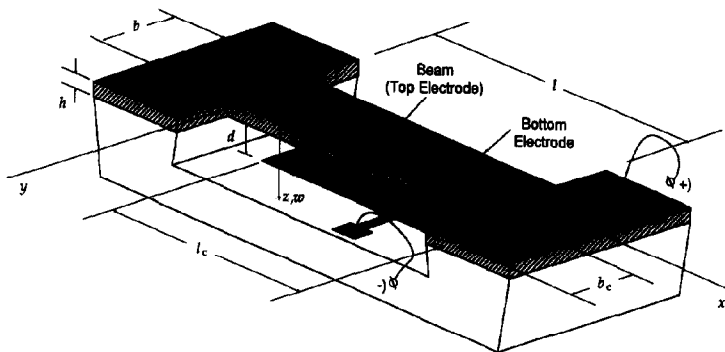


Fig. 3. Schematic drawing of a beam (length l , width b and thickness h) configured as a one-port resonator. The lower (stationary) electrode has a rectangular shape (length l_c and width b_c) and is placed concentric with the beam surface. The beam itself is homogeneous and is composed of a conducting material.

$$U_b = \frac{1}{2} \int_0^l \hat{E} I \left[\frac{d^2 \bar{w}^0(x)}{dx^2} \right]^2 dx$$

$$= \frac{1}{2} \int_0^l \hat{E} I \left[\sum_{i=1}^n a_i \frac{d^2 g_i(x)}{dx^2} \right]^2 dx \quad (4)$$

$$U_m = \frac{1}{2} \int_0^l N \left[\frac{d \bar{w}^0(x)}{dx} \right]^2 dx = \frac{1}{2} \int_0^l N \left[\sum_{i=1}^n a_i \frac{d g_i(x)}{dx} \right]^2 dx \quad (5)$$

$$V_{el} = - \int_0^l \left[\int_0^{w^0(x)} q_0(w^0(x), V_P) dw^0 \right] dx$$

$$= - \frac{1}{2} \epsilon_0 V_P^2 \int_0^l \int_b \frac{S(x,y)}{d - \sum_{i=1}^n a_i g_i(x)} dy dx \quad (6)$$

where l denotes the beam length. The principle of stationary potential energy now requires that at equilibrium $\partial \Pi / \partial a_i = 0$ for all i . This yields values for the coefficients a_i , and using Eq. (2) the static deflection profile can be determined. More details can be found in [12].

The attractive electrostatic force $q_0(w^0(x), V_P)$ is inversely proportional to the square of the gap spacing. The restoring force is formed by the bending and the membrane (or stretching) stiffness of the beam. At equilibrium, the electrostatic force is counterbalanced by the restoring force and the net force equals zero. An increase of the polarization voltage results in an increase of the electrostatic force, leading to an increase of the beam deflection and thus a decrease of the gap spacing. The latter decrease will lead to an additional increase of the electrostatic force. Or in other words, this is a system with positive feedback. As in any other system with positive feedback, a chance for instability exists which can be described as follows. If the polarization voltage exceeds the so-called pull-in voltage V_{PI} , the restoring force is no longer able to counterbalance the electrostatic force and the gap spacing immediately goes to zero; the system has become mechanically unstable. Whether an equilibrium is stable or unstable is determined by the second variation of the total potential energy [21]. For a stable equilibrium, the total potential energy must be at a (local) minimum, implying that the second variation must be positive definite. If this condition is not satisfied, the equilibrium is unstable. As long as $V_P < V_{PI}$, the second variation is positive definite at the equilibrium position. If $V_P > V_{PI}$, the second variation ceases to be positive definite. The pull-in voltage is clearly a critical value. The second variation ceases to be positive definite exactly when

$V_P = V_{PI}$. Thus, pull-in is defined as the condition where the second variation of the total potential energy equals zero. If the series expansion is truncated to one term, i.e., $\bar{w}^0(x) = a_1 g_1(x)$, this condition can be expressed as $\partial^2 \Pi / \partial a_1^2 = 0$.

At the onset of pull-in, both the first and the second variation of the total potential energy are zero. If the series expansion is truncated to one term, i.e., $\bar{w}^0(x) = a_1 g_1(x)$, a straightforward analysis using the conditions $\partial \Pi / \partial a_1 = 0$ and $\partial^2 \Pi / \partial a_1^2 = 0$, in conjunction with Eqs. (3)–(6), yields the following expression of the pull-in voltage [12]:

$$V_{PI} = \left[\frac{\int_0^l \hat{E} I g_{1,xx}^2(x) dx + \int_0^l N g_{1,x}^2(x) dx}{\epsilon_0 \iint \frac{S(x,y) g_1^2(x)}{[d - a_1^{PI} g_1(x)]^3} dy dx} \right]^{1/2} \quad (7)$$

where a comma followed by the space coordinate x indicates partial differentiation with respect to x and a_1^{PI} denotes the coefficient at pull-in, which can be obtained from the following implicit equation:

$$a_1 \iint \frac{S(x,y) g_1^2(x)}{[d - a_1 g_1(x)]^3} dy dx$$

$$- \frac{1}{2} \iint \frac{S(x,y) g_1(x)}{[d - a_1 g_1(x)]^2} dy dx = 0 \Rightarrow a_1 = a_1^{PI} \quad (8)$$

Note that the pull-in voltage not only depends on the axial force and the bending stiffness, but also on the active electrode area described by the function $S(x,y)$. In general, it is found that the pull-in voltage increases with decreasing electrode area (see also Fig. 4), with increasing tensile axial load and with increasing bending stiffness.

3.2. Admissible trial functions

Admissible trial functions are functions that are differentiable half as many times as the order of the system and satisfy the geometric boundary conditions of the problem [21,22]. If the natural boundary conditions are satisfied as well, the trial functions are better in the sense that fewer terms in the series expansion are needed to achieve a close agreement with the exact shape. Trigonometric functions turn out to be very convenient in solving the problem of a clamped–clamped beam. If the problem is restricted to symmetric electrode configurations with respect to the centre ($x = l/2$) of the beam, the following functions provide a suitable set of trigonometric trial functions:

$$g_i(x) = 1 - \cos(2i\pi x/l) \quad (9a)$$

Another convenient set of trial functions in solving the problem of a clamped–clamped beam is the mode shape functions or eigenfunctions of the beam, evaluated for

zero axial load (i.e., $N=0$) [11,12,21,22]:

$$g_i(x) = 1.259 \{ \cos(k_i x) - \cosh(k_i x) + \frac{\cos(k_i l) - \cosh(k_i l)}{\sinh(k_i l) - \sin(k_i l)} [\sin(k_i x) - \sinh(k_i x)] \} \quad (9b)$$

where the k_i denote constants that are determined by the order of the mode (e.g., $k_1 l \approx 4.730$ for a clamped-clamped beam) [11], and the coefficient 1.259 is introduced for scaling purposes, such that $g_1(l/2) = 2$.

3.3. Rectangular electrodes

The analysis of a homogeneous (clamped-clamped) beam resonator with a rectangular electrode, having a length l_c and width b_c , which is concentric with the beam surface, is of particular practical importance. For the special case where the active electrode area is given by the entire beam surface, i.e., $l_c = l$ and $b_c = b$ and thus $S(x,y) = 1$, the theoretical analysis is greatly simplified. If in addition the expansion given by Eq. (2) is truncated to a single term, the pull-in equations as expressed by Eqs. (7) and (8) apply. Simultaneously solving this set of equations leads to the following expressions for the pull-in voltage V_{PI0} (the subscript zero indicates a uniform electrode) and the corresponding coefficient a_1^{PI0} :

$$V_{PI0} \approx \frac{c_1 \pi^2}{l^2} \left(\frac{\hat{E} l d^3}{b \epsilon_0} \left(1 + c_2 \frac{N l^2}{\hat{E} I} \right) \right)^{1/2} \quad (10)$$

and

$$a_1^{PI0} = c_3 d \text{ for } l_c = l \text{ and } b_c = b \quad (11)$$

where c_1 , c_2 and c_3 are constants, depending on the choice of the trial function $g_1(x)$. Taking the trigonometric shape given by Eq. (9a) as a trial function, the values are: $c_1 = (1.92/0.6)^{1/2} \approx 1.220$, $c_2 = 1/4 \pi^2 \approx 0.0253$ and $c_3 = 0.200$. If the mode shape given by Eq. (9b) is used as a trial function, the following values for the constants are obtained: $c_1 \approx 1.199$, $c_2 = \gamma_1/12 \approx 0.0246$ (where $\gamma_1 \approx 0.295$ [11], see also Eq. (21)) and $c_3 \approx 0.199$. This example illustrates that the choice of the trial function has little influence on the resulting constants. It is evident that the maximum deflection w_{max}^0 occurs at the centre of the beam and is given by $w_{max}^0 = 2a_1$. Hence, the above indicates that pull-in occurs if the centre deflection approaches $0.4d$.

Eqs. (10)–(11) were derived for the special case where the active electrode area is given by the entire beam surface, i.e., $l_c = l$ and $b_c = b$. For partially overlapping electrodes the results change (slightly). Fig. 4 illustrates the effect a partial rectangularly shaped concentric electrode has on the pull-in voltage and on the maximum deflection at pull-in. The graph clearly

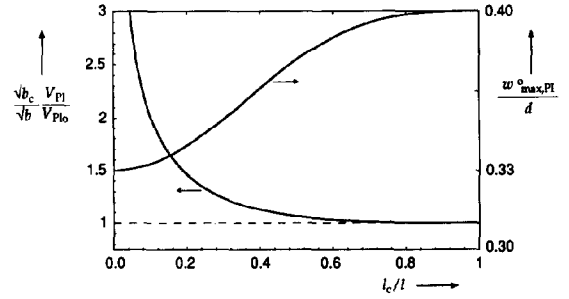


Fig. 4. The normalized pull-in voltage, $\sqrt{b_c} V_{PI} / \sqrt{b} V_{PI0}$, and the normalized maximum deflection at pull-in, $w_{max,PI}^0 / d$, vs. the fractional electrode length l_c/l . It is noted that the maximum deflection at pull-in is independent of the fractional width b_c/b of the electrode. The results are obtained using trigonometric trial functions given by Eq. (9a) and truncating the expansion of Eq. (2) to a single term.

illustrates that the pull-in voltage increases with decreasing electrode area. Further, at pull-in it is found that if l_c approaches zero, the normalized maximum deflection approaches $1/3$, i.e., the normalized deflection of a simple spring-mass system at pull-in [14,19].

It is pointed out that more accurate results are obtained if more than one term is included in the series expansion. However, this implies tedious mathematics in order to reach a solution. The fact that the results obtained with the energy method using a single term in the expansion are in close agreement with the results obtained from a numerical iterative solution of the differential equation of equilibrium [19] justifies the truncation to a single term. Moreover, in the following section it will turn out that the theory based on a single term in the expansion and the experiments are in very close agreement.

3.4. Dynamic behaviour

For small motions about the equilibrium position, $w(x,t) \ll d - w^0(x)$, and for small a.c. voltages, $v(t) \ll V_P$, the following linearized equation of motion can be derived [12]:

$$\hat{E} I \frac{\partial^4 w(x,t)}{\partial x^4} - N \frac{\partial^2 w(x,t)}{\partial x^2} + c \frac{\partial w(x,t)}{\partial t} + \rho A \frac{\partial^2 w(x,t)}{\partial t^2} = \frac{1}{2} \epsilon_0 \int_b S(x,y) dy \left\{ \frac{2V_P v(t)}{[d - w^0(x)]^2} + \frac{2V_P^2 w(x,t)}{[d - w^0(x)]^3} \right\} \quad (12)$$

where ρ denotes the specific mass of the beam material, $A = bh$ denotes the area of the beam cross section, $w(x,t)$ denotes the deflection about the equilibrium position defined by $w^0(x)$, $v(t)$ denotes the a.c. excitation voltage and c the viscous drag parameter, which is used to represent damping. Viscoelastic material damping is also easily accounted for by making Young's modulus

complex [12]. This will not change the following analysis significantly and as a matter of convenience will be omitted here. The first term on the right represents the actual electrostatic driving force, whereas the second term represents an ‘enhancement force’ that is due to the electromechanical coupling. The effect of the enhancement force is similar to the effect of the restoring force of an elastic foundation with a negative foundation modulus.

3.5. The fundamental frequency: Rayleigh’s quotient

The fundamental series resonance frequency ω_s can be obtained from Rayleigh’s quotient as follows [21,22]:

$$\omega_s^2 = \frac{\int_0^l \phi_1(x) \mathcal{L}[\phi_1(x)] dx}{\int_0^l \rho A \phi_1^2(x) dx} \quad (13)$$

where $\phi_1(x)$ denotes the eigenfunction or mode shape function of the fundamental mode and \mathcal{L} denotes the linear differential operator associated with Eq. (12):

$$\begin{aligned} \mathcal{L} &= \hat{E}I \frac{\partial^4}{\partial x^4} - N \frac{\partial^2}{\partial x^2} - \int_b \frac{\epsilon_0 V_F^2 S(x,y)}{[d - w^0(x)]^3} dy \\ &\equiv \hat{E}I \frac{\partial^4}{\partial x^4} - N \frac{\partial^2}{\partial x^2} - k(x) \end{aligned} \quad (14)$$

where $k(x)$ denotes a spring constant that is clearly defined by the equation above. It is pointed out that the term $-k(x)$ is added to the usual differential operator of the beam as a result of the electromechanical coupling. Further, it is noted that the eigenmodes are the solutions to the special eigenvalue problem [12,21,22] $\mathcal{L}[\phi(x)] = \lambda \rho A \phi(x)$, where λ denotes the eigenvalue corresponding to the eigenfunction ϕ . Using the boundary conditions of a clamped–clamped beam and introducing Eq. (14) into Eq. (13), the Rayleigh quotient can be written as follows:

$$\begin{aligned} \omega_s^2 &= \left\{ \int_0^l \hat{E}I \left[\frac{\partial^2 \phi_1(x)}{\partial x^2} \right]^2 dx + \int_0^l N \left[\frac{\partial \phi_1(x)}{\partial x} \right]^2 dx \right. \\ &\quad \left. - \int_0^l \frac{\epsilon_0 V_F^2 \phi_1^2(x)}{[d - w^0(x)]^3} \int_b S(x,y) dy dx \right\} / \\ &\quad \left[\int_0^l \rho A \phi_1^2(x) dx \right]^{-1} \end{aligned} \quad (15)$$

An exact value for the fundamental frequency is difficult to obtain, since this requires an exact expression for the fundamental mode shape. It can be shown that

Eq. (15) gives a good approximation for the fundamental frequency if, in place of $\phi_1(x)$, a function $\tilde{\phi}_1$ is used that on the one hand satisfies the boundary conditions and on the other hand reasonably resembles the fundamental mode shape [21,22]. Thus by using $\tilde{\phi}_1$ in the Rayleigh quotient, an approximate frequency $\tilde{\omega}_s$ is obtained. Further, it can be shown that $\tilde{\omega}_s$ always provides an upper bound, i.e., $\tilde{\omega}_s \geq \omega_s$ [21,22].

3.6. The electric admittance equivalent circuit

If the resonator is operated in a one-port configuration, the dynamic behaviour is fully described by the electric one-port admittance $Y(j\omega)$, where ω denotes the driving frequency of the sinusoidal drive: $v(t) = v \exp(j\omega t)$. The solution to the equation of equilibrium (12) is conveniently obtained using modal analysis [22]. Based on such an analysis, an expression for the admittance can be obtained [12,18]. In a narrow frequency regime around the fundamental series resonance, $Y(j\omega)$ can be approximated as

$$Y(j\omega) \equiv \frac{i}{v} \approx j\omega C_0 + \frac{j\omega C_1}{1 + \frac{1}{Q_s} \left(\frac{j\omega}{\omega_s} \right) + \left(\frac{j\omega}{\omega_s} \right)^2} \quad (16)$$

where

$$C_0 = \iint \frac{\epsilon_0}{d - w^0(x)} S(x,y) dx dy \quad (17)$$

$$C_1 = \frac{\left[\iint \frac{\epsilon_0 V_F \phi_1(x)}{[d - w^0(x)]^2} S(x,y) dx dy \right]^2}{\omega_s^2 \int_0^l \rho A \phi_1^2(x) dx} \quad (18)$$

C_0 and C_1 denote the static and motional capacitances (associated with the fundamental mode), respectively, and Q_s denotes the quality factor associated with the fundamental series mode. The admittance given by Eq. (16) can be represented by the equivalent circuit shown in Fig. 5 (the influence of an external parallel capacitor C_p will be discussed in Section 3.7). Note that this same circuit is also used to model quartz crystals. The newly introduced circuit components are given by

$$L_1 = \frac{1}{\omega_s^2 C_1} \Rightarrow \omega_s = 1/(L_1 C_1)^{1/2} \quad (19a)$$

$$R_1 = \frac{1}{Q_s} \left(\frac{L_1}{C_1} \right)^{1/2} \quad (19b)$$

The static capacitance C_0 is a true electrical capacitance, whereas the $R_1 L_1 C_1$ series branch represents the mechanical behaviour. In effect, the motional capacitance C_1 , the inductor L_1 and the resistor R_1 are functions

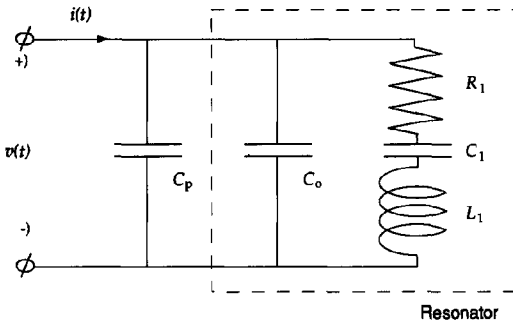


Fig. 5. Equivalent circuit representation of the electrostatic one-port resonator applicable in a narrow frequency regime around the fundamental mode. The capacitor C_p represents an external parasitic capacitor. The static capacitance C_0 is truly electrical in nature and represents the capacitance of the (air)gap capacitor. The $R_1 L_1 C_1$ series branch represents the motional behaviour associated with the fundamental mode. In effect, the motional capacitance C_1 , the inductor L_1 and the resistor R_1 are functions of the mechanical compliance of the resonator, the resonator mass and the mechanical losses, respectively [12].

of the mechanical compliance of the resonator, the resonator mass and the mechanical losses, respectively [12]. The subscript s stands for series, as opposed to parallel. Series resonance occurs if the inductor L_1 and the capacitor C_1 form a short circuit. The conductance (i.e., the real part of the admittance) displays a maximum at $\omega = \omega_s$. As a consequence of C_0 , a parallel resonance frequency ω_p exists at a slightly higher frequency than ω_s . At $\omega = \omega_p > \omega_s$ the resistance (i.e., real part of the impedance) displays a maximum. The parallel resonance frequency ω_p is given by (in the absence of external parallel loads)

$$\omega_p = \left[\frac{1}{L_1} \left(\frac{1}{C_1} + \frac{1}{C_0} \right) \right]^{1/2} \quad (20)$$

Oscillator circuitry can be designed to excite either resonance mode (series or parallel). It will be explained in the next section that the series resonance frequency is preferred as the frequency used to characterize the resonator.

More precisely, the existence of two resonance frequencies is due to the electromechanical coupling. The mechanical characteristics are not solely determined by the mechanical parameters, but also by the conditions at the electric port. In this context, the series resonance frequency is the resonance frequency defined for constant- v (also indicated as 'short-circuited') conditions at the electric port (i.e., voltage drive), while the parallel resonance frequency is defined for constant- q (also indicated as 'open-circuited') conditions at the electric port (i.e., current drive), where q denotes charge. As a matter of fact, for the system considered here, three fundamental resonance frequencies can be defined: ω_p , ω_s and ω_1 , where ω_1 is the resonance frequency of the system without electromechanical coupling ($V_P = 0$),

given by [11,12]

$$\omega_1 = 2\pi f_1 \approx \frac{\alpha_1^2}{l^2} \left(\frac{\hat{E}l}{\rho A} \right)^{1/2} \left(1 + \gamma_1 \frac{NI^2}{12EI} \right)^{1/2} \quad (21)$$

where α_1 and γ_1 are constants that are determined by the boundary conditions ($\alpha_1 \approx 4.730$ and $\gamma_1 \approx 0.295$ for a clamped-clamped beam). For a parallel-plate capacitor, ω_1 and ω_p are the same and the number of fundamental resonance frequencies reduces to two. A more extensive discussion dealing with the effects of electromechanical coupling can be found in [12].

3.7. Dependence on d.c. bias

The dependence of the series resonance frequency ω_s , the static capacitance C_0 and the motional capacitance C_1 on the polarization voltage V_P is expressed by Eqs. (15), (17) and (18), respectively. These expressions can be simplified and will become more mathematically tractable if the polarization voltage is much smaller than the pull-in voltage. In this case, the static deflection $w^0(x)$ can be neglected compared to the gap spacing d . Assuming a rectangular electrode, which is concentric with the beam surface (see Fig. 3), leads to the following simplified expressions for the series resonance frequency ω_s , the static capacitance C_0 (only evaluated for the special case when the active electrode area is given by the entire beam surface, i.e., $l_c = l$ and $b_c = b$) and the motional capacitance C_1 :

$$\begin{aligned} \omega_s &\approx \bar{\omega}_s \approx \omega_1 \left[1 - \frac{\epsilon_0 V_P^2 A_c}{\rho A l \omega_1^2 d^3} \frac{\chi_2}{\chi_3} \right]^{1/2} \\ &\approx \omega_1 \left[1 - \frac{c_1^2 \pi^4}{\alpha_1^4} \left(\frac{V_P}{V_{PI0}} \right)^2 \frac{A_c}{bl} \frac{\chi_2}{\chi_3} \right]^{1/2} \text{ for } V_P \ll V_{PI} \end{aligned} \quad (22)$$

$$\begin{aligned} C_0 &\approx \frac{C_{00}}{\left[1 - \frac{1}{8} c_1^2 \left(\frac{V_P}{V_{PI0}} \right)^2 \right]^{1/2}} \\ &\text{for } V_P \ll V_{PI0}, l_c = l \text{ and } b_c = b \end{aligned} \quad (23)$$

$$\begin{aligned} C_1 &\approx C_{00} \frac{\epsilon_0 V_P^2 A_c}{\rho A l \omega_1^2 d^3 (\bar{\omega}_s/\omega_1)^2} \frac{\chi_1^2}{\chi_3} \\ &\approx C_{00} \frac{c_1^2 \pi^4}{\alpha_1^4} \frac{A_c}{bl} \frac{(V_P/V_{PI0})^2}{(\bar{\omega}_s/\omega_1)^2} \frac{\chi_1^2}{\chi_3} \text{ for } V_P \ll V_{PI} \end{aligned} \quad (24)$$

C_{00} is defined by $C_{00} \equiv \epsilon_0 A_c/d$ and A_c denotes the active capacitor area, given by

$$A_c = \iint S(x,y) dx dy \longrightarrow b_c l_c \quad (25)$$

χ_1 , χ_2 and χ_3 are shape factors, respectively given by

$$\chi_1 = \frac{1}{A_c} \iint \tilde{\phi}_1(x) S(x, y) dx dy \longrightarrow \frac{1}{l_c} \int_{(l-l_c)/2}^{(l+l_c)/2} \tilde{\phi}_1(x) dx \quad (26)$$

$$\chi_2 = \frac{1}{A_c} \iint \tilde{\phi}_1^2(x) S(x, y) dx dy \longrightarrow \frac{1}{l_c} \int_{(l-l_c)/2}^{(l+l_c)/2} \tilde{\phi}_1^2(x) dx \quad (27)$$

$$\chi_3 = \frac{1}{l} \int_0^l \tilde{\phi}_1^2(x) dx \quad (28)$$

where the surface integrals are evaluated over the entire beam surface and the expressions following the arrows are obtained for a concentric rectangularly shaped active electrode as shown in Fig. 3. The d.c. bias dependence is graphically illustrated in Figs. 6 and 7(a,b) for the series resonance frequency ω_s , the static capacitance C_0 and the motional capacitance C_1 , respectively. As the approximate mode shape, $\tilde{\phi}_1(x)$, the eigenfunctions of a clamped-clamped beam with zero axial load ($N=0$) and no electromechanical coupling ($k(x)=0$) were used: $\tilde{\phi}_1(x)=g_1(x)/1.259$, where $g_1(x)$ is given by Eq. (9b). Note that for this choice of $\tilde{\phi}_1(x)$ the shape factor

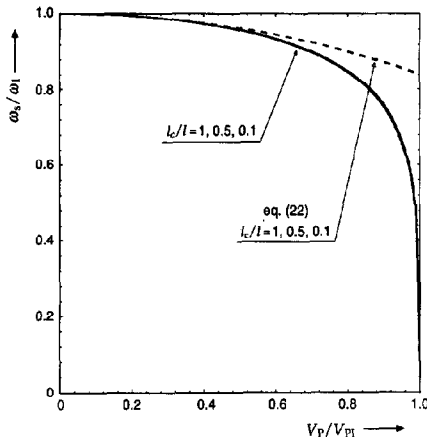


Fig. 6. Predicted normalized series resonance frequency ω_s/ω_1 vs. the normalized polarization voltage V_P/V_{PI} computed for a clamped-clamped beam and three different electrode lengths l_c ; ω_1 denotes the fundamental resonance frequency of the beam without electromechanical coupling, i.e., $V_P=0$ (see also Eq. (21)). Note that the curves for the different electrode lengths practically coincide. The dashed curves represent the approximations given by Eq. (22), whereby as an approximate mode shape, $\tilde{\phi}_1(x)$, the eigenfunctions of a clamped-clamped beam with zero axial load ($N=0$) and no electromechanical coupling were used: $\tilde{\phi}_1(x)=g_1(x)/1.259$, where $g_1(x)$ is given by Eq. (9b). The solid curves are obtained from a numerical solution of Eq. (15), using the same approximate mode shape for $\phi_1(x)$ as before, and for the static deflection profile the trigonometric trial function was used: $w^0(x)=g_1(x)$, where $g_1(x)$ is given by Eq. (9a).

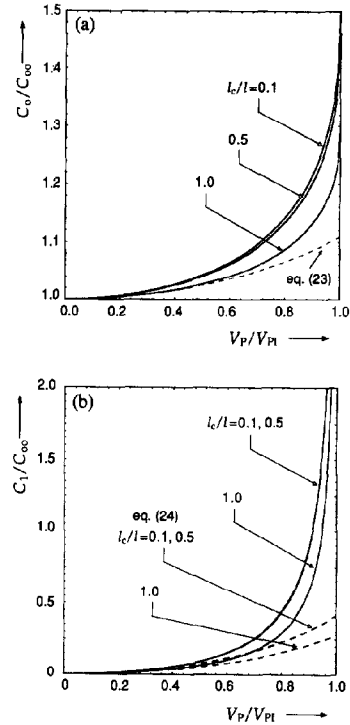


Fig. 7. Normalized capacitances vs. the normalized polarization voltage V_P/V_{PI} with the normalized electrode length l_c/l as parameter. The dashed curves represent the approximations given by Eqs. (23) and (24); as an approximate mode shape, $\tilde{\phi}_1(x)$, the eigenfunctions of a clamped-clamped beam with zero axial load ($N=0$) and no electromechanical coupling were used: $\tilde{\phi}_1(x)=g_1(x)/1.259$, where $g_1(x)$ is given by Eq. (9b). The solid curves are obtained from a numerical solution of Eqs. (17) and (18), using the same approximate mode shape for $\phi_1(x)$ as before, and for the static deflection profile the trigonometric trial function was used: $w^0(x)=g_1(x)$ where $g_1(x)$ is given by Eq. (9a). The reference capacitance is given by $C_{00}=\epsilon_0 b_e l_c/d$, and the pull-in voltage can be obtained from Fig. 4 in combination with Eq. (10)). (a) The normalized static capacitance C_0/C_{00} . The dashed curve represents the approximation given by Eq. (23). The solid curves are obtained from a numerical solution of Eq. (17). (b) The normalized motional capacitance C_1/C_{00} . The dashed curves are obtained using the approximate expressions given by Eq. (24). The solid curves are obtained from a numerical solution of Eq. (18).

$\chi_3=1$. For the static deflection profile, the first term of the series given by Eq. (2) using the trigonometric shape functions given by Eq. (9a) is used. The solid lines are obtained from a numerical evaluation of Eqs. (15), (17) and (18). The dashed curves indicate the approximations expressed by Eqs. (22), (23) and (24) which are only valid for small polarization voltages. It is seen in Fig. 6 that the series resonance frequency decreases with increasing V_P . This effect has been recognized and experimentally observed by many authors in the past [9,14–16,18,19]. Both the motional capacitance C_1 and the static capacitance C_0 increase with increasing polarization voltage. If the polarization voltage equals the pull-in voltage, the series resonance

frequency is exactly zero and the motional capacitance C_1 approaches infinity.

In Fig. 6, the curves computed for the different electrode lengths l_c practically coincide. In this context it is pointed out that the pull-in voltage is a function of l_c (see Fig. 4), which is reflected as a rescaling of the horizontal axis. It is further pointed out that the parallel resonance frequency ω_p given by Eq. (20) also decreases with increasing polarization voltage (not shown). The effect that V_P has on the parallel resonance frequency is smaller, however. For a parallel-plate capacitor (and in the absence of any external parallel loads in addition to C_0)¹ there is even no influence of V_P on ω_p at all. This suggests that the parallel resonance frequency would provide a better output signal for a sensing device than the series resonance frequency. The series resonance frequency, however, is less susceptible to parasitic loads than the parallel resonance frequency. Note that ω_s (see Eq. (19a)) is independent of the parallel capacitors C_0 and C_p , where the latter denotes a parasitic parallel capacitance (see Fig. 5). The only parasitics that affect the series resonance frequency are series loads, but these loads are easily kept very small, and are therefore ignored. The only parasitic loads that are of importance for the electrostatically driven resonator are parallel loads. The parallel resonance frequency is partly determined by the capacitance C_p . This is easily seen from Eq. (20) by replacing C_0 by $C_0 + C_p$. In effect, this means that in the case $C_p \gg C_0$ and for small polarization voltages, the bias dependence of the parallel resonance frequency practically follows the bias dependence of the series resonance frequency, thus removing the advantage of the lower susceptibility of the parallel mode to the polarization voltage. In addition, if a parallel-mode oscillator is employed, the variations in parasitic parallel capacitances must be kept to a minimum in order to avoid an erroneous frequency output. The above discussion clearly indicates that the series resonance frequency is generally preferred as the most suitable characteristic resonance frequency of the electrostat-

ically driven resonator, in particular if the latter is employed as a resonant strain gauge for sensing applications.

3.8. Large-amplitude effects

The resonance frequencies of a beam with rigidly fixed ends increase with increasing amplitude of the vibration: an effect known in the literature as the 'hard spring effect' [11,23,24]. Assuming a single degree of freedom, the amplitude of vibration w_{\max} at resonance can be obtained from the maximum (centre) static deflection w_{\max}^0 as follows:

$$w_{\max} \approx Q_s \frac{dw_{\max}^0}{dV_P} v \quad (29a)$$

or

$$\frac{w_{\max}}{h} \approx Q_s \frac{d}{h} \psi \frac{v}{V_{PI}} \quad (29b)$$

where v denotes the amplitude of the a.c. harmonic driving voltage and ψ denotes the sensitivity of w_{\max}^0 to changes in V_P , defined by

$$\psi \equiv \left. \frac{d(w_{\max}^0/d)}{d(V_P/V_{PI})} \right|_{\text{operating point}} \quad (30)$$

Using a trigonometric trial function of the form given by Eq. (9a) and truncating the expansion of Eq. (2) to the first term, it follows that for small polarization voltages and for a uniform electrode ($l_c = l$ and $b_c = b$), the sensitivity ψ can be expressed as [12]

$$\psi \approx \frac{2}{V_P/V_{PI0}} \frac{w_{\max}^0}{d} \quad (31a)$$

$$\approx \frac{\frac{1}{4} c_1^2 (V_P/V_{PI0})}{1 - \frac{3}{16} c_1^2 (V_P/V_{PI0})^2} \quad (31b)$$

$$\approx \frac{1}{4} c_1^2 \frac{V_P}{V_{PI0}} \quad (31c)$$

for $V_P \ll V_{PI0}$, $l_c = l$ and $b_c = b$. Both the 'exact' and the approximate forms of Eq. (31b,c) are shown in Fig. 8. For a uniform electrode ($l_c = l$ and $b_c = b$), the amplitude of vibration at resonance can conveniently be expressed in terms of the resonance frequency ω_1 as follows (from Eqs. (10), (21), (29b) and (31c)):

$$\begin{aligned} w_{\max} &\approx 0.37 Q_s d \frac{v V_P}{V_{PI0}^2} \\ &\approx 1.3 Q_s \epsilon_0 \frac{v V_P}{\rho h \omega_1^2 d^2} \text{ for } l_c = l \text{ and } b_c = b \end{aligned} \quad (32)$$

¹For the special case of a parallel-plate capacitor, the following relations can be derived:

$$\omega_p^2 = \frac{\omega_1^2}{1 + k_{em}^2 C_p/C_0} \text{ and } \omega_s^2 = \omega_p^2 (1 - k_{em}^2)$$

where

$$k_{em}^2 = \frac{\omega_p^2 - \omega_s^2}{\omega_p^2} = \frac{1}{1 + (C_0 + C_p)/C_1}$$

is the electromechanical coupling factor [12]. The above equations indicate that in the absence of external loads ($C_p = 0$), the parallel resonance frequency equals the resonance frequency ω_1 of the system without electromechanical coupling, whereas for very large parasitics ($C_p \gg C_0$) the three characteristic frequencies approach each other with a relative magnitude $\omega_s < \omega_p < \omega_1$.

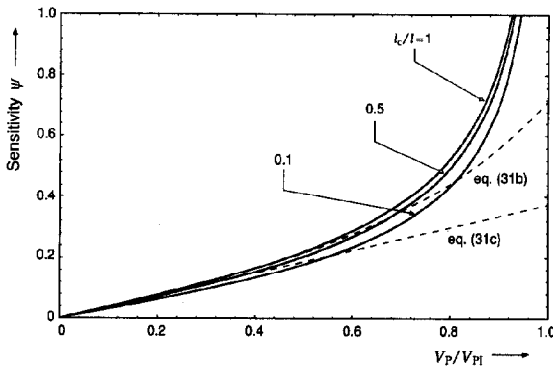


Fig. 8. Sensitivity ψ as defined by Eq. (30). The solid lines indicate the sensitivity obtained from a numerical routine for three different values of the electrode length. For the static deflection profile a trigonometric trial function was used, given by $w^0(x) = g_1(x)$, where $g_1(x)$ is given by Eq. (9a). The dashed lines indicate the approximate expressions given by Eqs. (31b,c), which were derived for the special case where the active electrode area is given by the entire beam surface, i.e., $l_c = l$ and $b_c = b$.

From the analysis presented in [11] in conjunction with Eq. (29b), the dependence of the resonance frequency on the a.c. driving voltage v can be derived, yielding,

$$\tilde{\omega}_1 \approx \omega_1 \left[1 + \frac{\hat{\beta}_1 Q_s^2 (d/h)^2 \psi^2 (v/V_{PI})^2}{1 + \hat{\gamma}_1 \epsilon (l/h)^2} \right]^{1/2} \quad (33)$$

where $\tilde{\omega}_1$ denotes the resonance frequency without electromechanical coupling, but including the large-amplitude effect, $\epsilon = N/(Ebh)$ denotes the axial (tensile) strain and the coefficient $\hat{\beta}_1 = \beta_1(1 - \nu^2)$ represents the amplitude stiffening effect [11] ($\beta_1 \approx 0.528$ for a prismatic clamped-clamped beam with a rectangular cross section). Eq. (33) indicates that the amplitude stiffening is more severe for a high quality factor, a high d.c. polarization voltage and high a.c. driving voltages. Large axial strains make the resonator less susceptible to the stiffening effect. This dependence is graphically illustrated in Fig. 9.

3.9. Influence of the surrounding gas in the narrow gap

The characteristics of an air-gap resonator are partly determined by squeeze-film effects of the gas present in the gap. Three effects can be distinguished: (1) *squeeze-film damping*, leading to a lowering of the mechanical quality factor and an apparent (rather small) decrease of the resonance frequency; (2) *gap stiffening*, leading to an increase of the resonance frequency; (3) *mass loading*, leading to a decrease of the resonance frequency. All three effects are strongly dependent on the gap spacing and the surrounding gas pressure. In general it can be said that the effects will only be significant for small gap spacings (i.e., (much) smaller than the lateral dimension of the resonator) and at

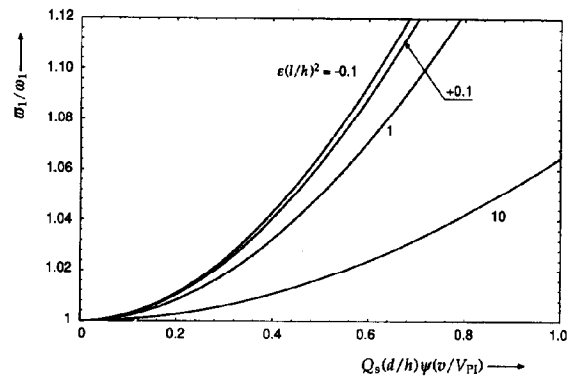


Fig. 9. Predicted dependence of the natural frequency on the amplitude of the a.c. driving voltage, with $\epsilon(l/h)^2$ as parameter (see Eq. (32)). The curves are computed for $\nu = 0$, $\beta_1 = 0.528$ and $\gamma_1 = 0.295$. Note that the effect of a partial active electrode area (l_c , b_c) is accounted for in the sensitivity ψ and the pull-in voltage V_{PI} .

sufficiently high pressures. Squeeze-film damping can be significant in a broad pressure range, varying from the molecular regime to the viscous regime. Measured data on the quality factor were reported in the accompanying paper [20] and have clearly demonstrated this effect. Gap stiffening is due to the spring-like behaviour of the trapped gas in the (narrow) gap. The additional (air)-spring raises the resonance frequency as compared to the resonance frequency in vacuum. This effect will be more pronounced at higher frequencies. This is easily conceived if one thinks in terms of the time that is allowed for the gas molecules to escape from underneath the gap. At high frequencies the escape time is short, which leads to compression of the gas and thus to an added stiffness. Mass loading is a result of ambient gas moving with the resonator, leading to an apparent increase of the resonator inertia or mass. Mass loading is to a certain extent independent of the gap spacing and only depends on the specific density (and thus pressure) of the surrounding gas molecules.

The above effects are not considered in further detail in this paper. This is justified by recalling that the surrounding gas pressure (≈ 0.1 – 0.2 mbar [20]) is very low. The only clearly noticeable effect is the lowering of the quality factor as compared to the predicted value for a resonator in free space. The emphasis in this paper, however, is on the resonance frequencies. Measured data of the resonance frequencies have not revealed any significant pressure dependence below pressures of 1 mbar. Similar observations were made by Andrews et al. [25]. They have studied both theoretically and experimentally the effects of squeezed films of gas on the dynamic characteristics of a microstructure consisting of two plates vibrating normal to each other.

4. Experiments and discussion

4.1. General

The experimental data presented in this section are extracted from resonators configured as a one-port according to scheme 1a (see Table 1). The frequency responses were measured using an HP4194A gain-phase analyser. The mechanical quality factor of a one-port resonator can be extracted from the measured Bode plot and is easily understood after an inspection of Eq. (16) and Eq. (19b) [12]. Data of the Q -factor dependence on geometry and pressure are presented in the accompanying paper [20].

The resonator behaviour is considered to be linear if the resonator stiffening due to the hard spring effect can be neglected. In general this is achieved if the a.c. drive voltage v and the d.c. polarization voltage V_p are not too high (see Eqs. (31c) and (33)). In this context, a compromise is sought between the maximum acceptable distortion as a result of the hard spring effect and the noise level. Further, in the previous section it was shown that gap stiffening and mass loading can be ignored.

4.2. Typical frequency response

Fig. 10 compares a typical measured admittance plot of a resonator (with code A210) having a length of 210 μm with the model of Fig. 5. The conductance is slightly negative far away from the resonance frequency. This is due to noise generated in the sample and to light acting as an external energy source. It is found

that apart from this discrepancy, the equivalent circuit accurately models the electromechanical behaviour of the resonator. The parameters of the one-port model used to calculate the response were obtained from a best fit of the predicted and the measured responses. This resulted in the following extracted parameter values: $C_1 = 1.4252$ fF, $L_1 = 169.64$ H, $R_1 = 582.780$ k Ω and $C_0 + C_p = 0.39$ pF. This gives an extracted series resonance frequency (i.e., the frequency where the conductance displays a maximum) $f_s \approx 323\,682$ Hz and a quality factor $Q_s \approx 592$. The resonator electromechanical coupling factor k_{em} ($\approx [C_1/(C_0 + C_p)]^{1/2}$) is 0.06 and its figure of merit \mathcal{M} is 2.16 [12]. The coupling factor is a measure for the electromechanical energy conversion. For a stable equilibrium, the coupling factor always has a value between zero and one: $0 < k_{em} < 1$. A coupling factor of zero means no electromechanical interaction at all. The higher the coupling factor, the more pronounced the electromechanical interaction will be. At pull-in, the coupling factor approaches unity. Note that an external parallel capacitor C_p (see Fig. 5) will lower the coupling factor. The figure of merit \mathcal{M} is strongly related to the coupling factor and can approximately be expressed as $\mathcal{M} = Q_s k_{em}^2$ [12]. It is seen that the figure of merit effectively combines the mechanical quality factor and the electromechanical coupling factor into a single measure. The figure of merit is a measure of the relative contribution of the motional admittance to the overall admittance [12]. Larger values for \mathcal{M} mean easier detection of the resonance. As a rule of thumb, it can be said that a figure of merit greater than unity means a rather strong and easily detectable resonance. To facilitate the electronics of the sustaining oscillator, however, a figure of merit larger than 10 is recommended. This is because the admittance should have a clearly distinguishable inductive region, i.e., a region where the susceptance is negative. The admittance will have an inductive region for $\mathcal{M} > 2$, otherwise its behaviour will always be capacitive [12]. It is also pointed out that a larger coupling factor indeed means a strong electromechanical interaction, but, if the quality factor is very low the resonance might still be very weak. Thus, the figure of merit is considered to be of more significance as a performance characteristic for studying the resonance characteristics than the quality factor or the coupling factor. For the electrostatically driven resonator, the figure of merit can be raised by increasing the polarization voltage and the quality factor and/or by lowering the external parallel capacitance [12]. The latter approach is preferred, since increasing the polarization voltage will also lead to undesirable amplitude effects (see also Sections 3.8 and 4.5).

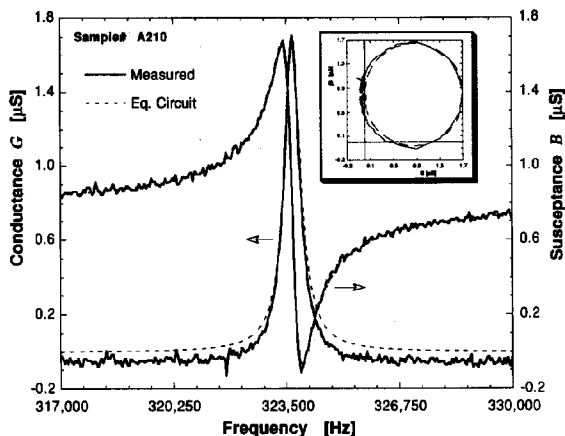


Fig. 10. Measured and calculated responses of microbridge A210, having a length of 210 μm , a width of 100 μm , a thickness of 1.50 μm and a gap spacing of 1.18 μm . The interconnection is according to scheme 1a of Table 1. The d.c. polarization voltage was equal to 6.0 V and the a.c. drive voltage was equal to 0.01 V. The dashed lines indicate the response function of the one-port network of Fig. 5 using the following parameter values: $C_1 = 1.4252$ fF, $L_1 = 169.64$ H, $R_1 = 582.780$ k Ω and $C_0 + C_p = 0.39$ pF.

4.3. Extraction of material parameters

The plate modulus $E/(1-\nu^2)$ and the residual strain can be found by measuring the resonance frequency of microbridges of varying length. To get an idea of the spread across the wafer and to minimize the measurement error, the fundamental frequency was measured on 10 locations, uniformly distributed over the wafer. The average value of the measured mode frequencies together with the standard deviations across the wafer are given in Table 2. Both the measured series resonance frequency $f_s = \omega_s/2\pi$ and the calculated resonance frequency $f_1 = \omega_1/2\pi$ (shown in parentheses) are given. As indicated before, it is expected that no corrections are necessary to account for squeezed-film effects. Table 2 also gives the measured pull-in voltages of resonators A210, A310, A410 and A510 (see also Section 4.4), together with the measurement error.

Resonance frequency data of the four beams with different lengths are used to determine the residual strain and the plate modulus [26]. Two beams of different length are in principle enough to find the two unknowns. But in order to reduce the measurement error, it is better to use all four available beam lengths. Eq. (21) for the fundamental frequency is rewritten as follows:

$$(f_1 l)^2 = \frac{\alpha_1^4}{48\pi^2} \frac{E/(1-\nu^2)}{\rho} \left[\left(\frac{h}{l} \right)^2 + \gamma_1 \epsilon_0 (1-\nu^2) \right] \quad (34)$$

where ϵ_0 denotes the residual strain. The graph of $(f_1 l)^2$ as a function of $(h/l)^2$ is plotted in Fig. 11. The straight line is determined by a least-square fit.

Eq. (34) indicates that the plate modulus can be obtained from the slope, and the effective residual strain from the zero offset. Using $\alpha_1 = 4.730$, $\gamma_1 = 0.295$ and $\rho = 2332 \text{ kg m}^{-3}$, yields the following parameter values for thermally annealed (1 h at 1000 °C in a nitrogen ambient) boron-doped (dose = 10^{16} cm^{-2} , energy = 150 keV) LPCVD (590 °C, 50 sccm SiH_4 , 250 mTorr) polysilicon:

$$\frac{E}{(1-\nu^2)} = 166 \text{ GPa} \quad (35a)$$

$$\epsilon_0(1-\nu^2) = +36.8 \text{ ppm (tensile)} \quad (35b)$$

Assuming $\nu = 0.3$, estimates of 151 GPa and of 40.4 ppm are obtained for Young's modulus and the residual strain, respectively. This value for Young's modulus is 73% more than that reported for boron-doped polysilicon by Putty et al. [16], but within a few percent of the value reported by Zook et al. [4]. The value of the residual strain lies within the strain range as found from the ring- and buckled-beam diagnostic structures [20].

4.4. D.c. bias dependence: pull-in

In Section 3.2 it was explained that the fundamental series resonance frequency $\omega_s = 2\pi f_s$, the static capacitance C_0 and the motional capacitance C_1 are functions of the d.c. polarization voltage V_p . Fig. 12 compares the measured frequency dependence with the theoretical dependence as predicted by Eq. (22) for all four resonator lengths. It is found that the model given by Eq. (22) shows excellent agreement with the experiments for small polarization voltages.

The pull-in voltages can be determined by extrapolating the above graphs to zero frequency. Another method is based on the d.c. bias dependence of the static capacitance. A graph of the static capacitance of beam A210 as a function of the d.c. bias is shown in Fig. 13. At pull-in (close to 28 V), the gap spacing immediately goes to a very small value, which is determined by the thickness of the nitride sealing layer. In general the pull-in voltage exceeds the breakdown voltage of the nitride layer, resulting in a short circuit. For all beam lengths, it was found that values for the pull-in voltage extracted from static measurements of the type shown in Fig. 13 coincide with the values

Table 2

Measured average resonance frequencies (f_s and f_3) and pull-in voltages for four different beam lengths. The beam width is 100 μm , the thickness is 1.50 μm and the gap spacing is 1.18 μm . The second column gives the d.c. polarization voltage. The a.c. voltage is kept small so that the hard spring effect can be ignored. The standard deviation in the fundamental frequency f_s is obtained from 10 measurements across the wafer and for the second overtone f_3 from five measurements across the wafer. The values in parentheses denote the calculated fundamental frequency f_1 , obtained after extrapolating according to Eq. (22), substituting $c_1 = 1.22$, $\alpha_1 = 4.730$ and the pull-in voltage given in the last column. The pull-in voltage was only measured on one location (i.e., resonators A210, A310, A410 and A510) and the spread in the pull-in voltage is due to a measurement error. The measurement error in the mode frequencies is much smaller than the standard deviation and is not taken into account

Length (μm)	D.c. bias (V)	Fundamental frequency (kHz)	2nd overtone (kHz)	Pull-in voltage (V)
210	6.0	322.045 (324.214) ± 2.883	1624.092 ± 6.677	27.95 ± 0.05
310	3.0	163.215 (164.347) ± 3.962	762.350 ± 4.729	13.78 ± 0.03
410	3.0	102.169 (103.804) ± 2.791	453.390 ± 4.415	9.13 ± 0.02
510	2.0	73.791 (74.8024) ± 2.475	306.225 ± 3.019	6.57 ± 0.02

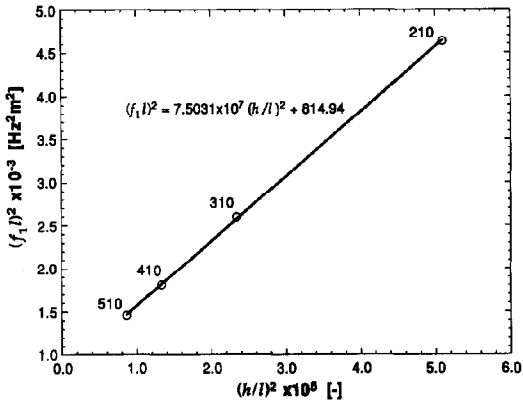


Fig. 11. Plot showing $(f_1/l)^2$ as a function of $(h/l)^2$ for the four different beam lengths indicated in Table 2. The correlation coefficient of the least-square linear fit is 0.99994.

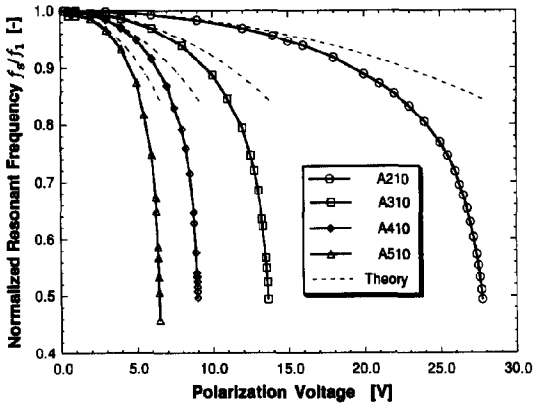


Fig. 12. Normalized fundamental frequency f_1/f_1 vs. the d.c. polarization voltage V_p of resonators A210, A310, A410 and A510. The dashed lines are computed using Eq. (22), evaluated for the pull-in voltages indicated in Table 2.

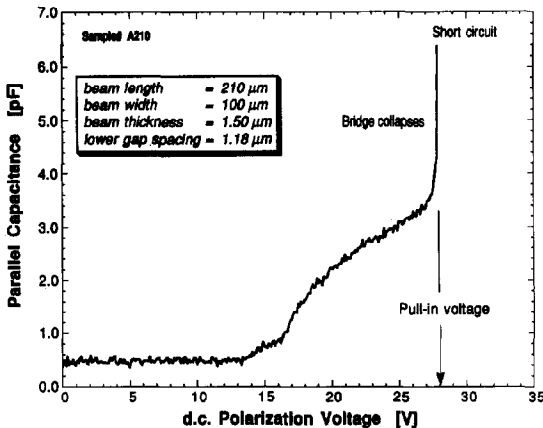


Fig. 13. Measured static parallel capacitance ($C_0 + C_p$) vs. the polarization voltage V_p for resonator A210. Pull-in occurs between 27.9 and 28.0 V (the step interval was 0.1 V).

extracted from dynamic measurements of the type shown in Fig. 12.

More data of resonators A210, A310, A410 and A510 are presented in Table 3, which also compares experimental data with the theoretical values (shown in parentheses). A good agreement (within a few percent) is found between the theory and the experiment. It is further noted that the d.c. bias dependence of C_1 is in agreement with the theory as expressed by Eq. (24). Discrepancies between theory and experiment are attributed to approximations made in deriving the mathematical models and to uncertainties in the geometric and material parameters. For instance, the assumption of perfectly clamped edges is not true. Finite-element computations performed on doubly-supported beams with 'step-up' boundaries indicated values for the resonance frequencies that are somewhat smaller than those predicted by the model assuming perfectly clamped edges. The deviation increases with decreasing beam length. For the 210 μm long beam, a deviation of 2% was found. This means that the extracted value for the plate modulus as given by Eq. (35a) indicates a lower estimate. Similar results for step-up beams that were based on static deflections were found by Mullen et al. [27]. Errors in the thickness, length and width of the beams also cause discrepancies. The length in particular has a strong influence. For instance, choosing a length of 507 μm instead of 510 μm results in a change of the predicted value for the pull-in voltage from 6.52 to 6.57 V, which brings the theory into excellent agreement with the experiments.

4.5. Non-linear behaviour (hard spring effect)

In the previous section, very small a.c. drive voltages were used. As indicated in Section 3.8, the resonance frequency shifts to higher values if the driving voltage is increased, an effect known as the hard spring effect [11,23,24]. The influence of the a.c. drive voltage on the measured conductance is illustrated in Fig. 14. The hysteresis interval is clearly seen and the characteristic jump phenomenon was clearly observed. Eq. (32) predicts peak deflections at resonance of approximately 24 and 71 nm for a.c. driving voltages of 10 and 30 mV, respectively. This example illustrates that the hard spring effect already shows up for peak deflections that are much smaller (less than 6%) than the beam thickness (1.5 μm) and the gap spacing (1.2 μm). Or in other words, the vibrational motion will hardly affect the true electrical capacitance. This illustrates once more that the change of the electric capacitance is not responsible for the resonance phenomena. The latter are entirely due to the coupling between the electric and mechanical energy domains. This is easily conceived from an inspection of the characteristics of the equivalent circuit of Fig. 5. At series resonance, the motional capacitance

Table 3

Measured and calculated parameter values of resonators A210, A310, A410 and A510. For all resonators the width $b=b_c=100\text{ }\mu\text{m}$, thickness $h=1.50\text{ }\mu\text{m}$ and zero-voltage gap spacing $d=1.18\text{ }\mu\text{m}$. Further, the values used for the plate modulus and effective residual strain are given by Eq. (35a,b). The calculated values are shown in parentheses and are based on the trigonometric trial functions given by Eq. (9a) and the expansion given by Eq. (2) is truncated to a single term. The first value in parentheses of C_1 is based on the measured value of the pull-in voltage, while the second value uses the calculated value for the pull-in voltage

#	l (μm)	l_c (μm)	V_P (V)	V_{PI} (V) Eq. (10)	C_1 (fF) Eq. (24)	f_s (kHz) Eq. (22)	Q	\mathcal{A}
A210	210	180	6.0	28.0 (28.0)	1.43 (1.45, 1.45)	323.7 (322.3)	592	2.16
A310	310	280	2.0	13.8 (14.2)	0.91 (0.98, 0.92)	161.8 (163.1)	151	0.30
A410	410	380	3.0	9.13 (9.02)	6.81 (6.84, 7.01)	101.4 (102.4)	45	0.49
A510	510	480	2.0	6.57 (6.52)	8.81 (7.29, 7.39)	72.38 (74.01)	30	0.36

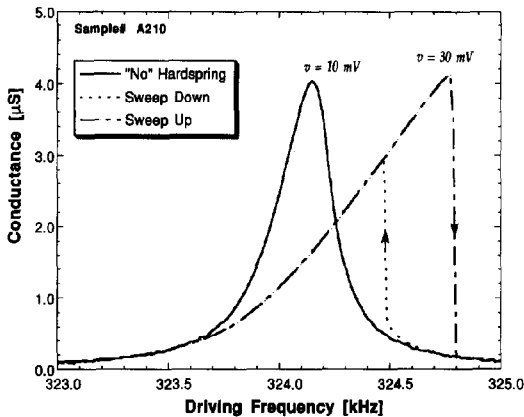


Fig. 14. Bode plot of the conductance of a $210\text{ }\mu\text{m}$ long beam (sample A210, see also Table 3), illustrating the hard spring effect. The hysteresis is clearly seen. The d.c. voltage in all three cases was 7 V and the a.c. voltage was 10 mV for the case with little visible hard spring effect and 30 mV for the two cases with significant hard spring effect.

and inductance form a short circuit, leading to a (sharp) increase of the conductance. This is clearly independent of the static capacitance, as long as the resistance R_1 is not excessively large. As a matter of fact, the theory used to derive the equivalent circuit of Fig. 5 assumes (infinitesimal) small deflections and does not take non-linear effects into account.

Graphs of the series resonance frequency as a function of the a.c. drive voltage for two different beam lengths are shown in Fig. 15. The graphs indicate that the theory given by Eq. (33) is qualitatively in good agreement with the experiments; the square-root behaviour is clearly observed. Quantitatively the agreement cannot be designated as being good. The discrepancy between the theory and the experiments will be practically removed, if instead of 0.528 a value within the range 0.7–0.9 is substituted for the coefficient β_1 . Reasons for the discrepancy are not quite clear at the moment, but possible explanations are errors in the values of the parameters (e.g., Q_s , β_1 or d/h) of Eq. (33).

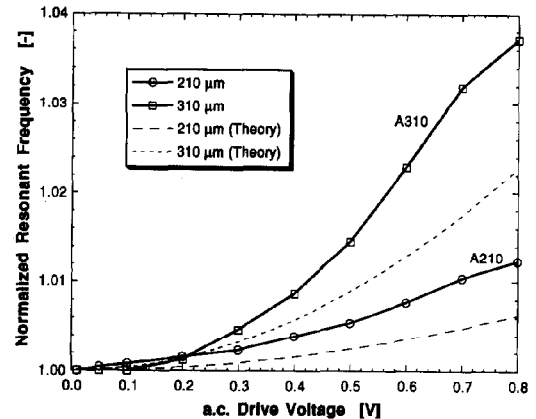


Fig. 15. Normalized resonance frequency vs. the a.c. drive voltage for resonators A210 and A310. The d.c. polarization voltage was 2 V for all data points of A310 and for the first three data points of A210. The other data points of A210 were measured with a polarization voltage of 1 V. The dashed curves are computed using Eq. (33) (see also Fig. 9), taking $\beta_1=0.528$ and $\nu=0.30$.

4.6. Strain sensitivity

The strain sensitivity was measured using a micrometer-driven four-point bending-beam deflection jig as shown in the inset of Fig. 16. A displacement instead of a force is applied to the load bar, since the former requires no knowledge about the material properties of the sensor beam while calculating the induced strain from the externally applied load. Fig. 16 shows the resonance frequency squared as a function of the applied displacement for two different beam lengths. The axial strain induced in the resonator is related to the displacement as follows [28]:

$$\epsilon_s = S_s \delta_t = S_s (\delta_0 + \delta) \quad (36a)$$

where

$$S_s = \frac{h_s}{La} \frac{1}{(1+2a/3L)} \quad (36b)$$

δ_t denotes the total applied displacement, S_s denotes the conversion factor from displacement to strain, h_s

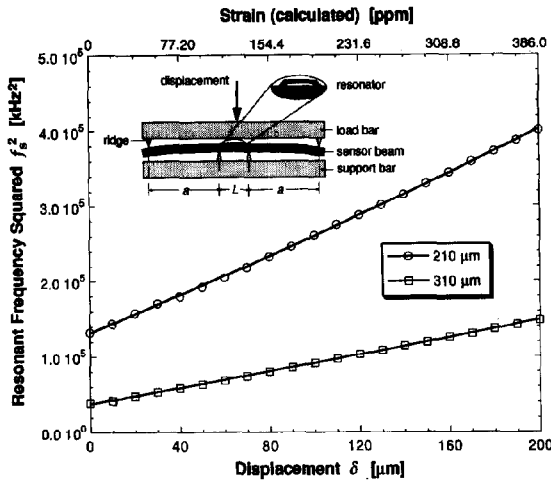


Fig. 16. Fundamental resonance frequencies squared, of 210 and 310 μm long beams, vs. the applied displacement. A four-point bending-beam deflection jig was used for the measurements. The dimensional parameters are $a = 15$ mm, $h_s = 0.406$ mm and $L = 4$ mm. The induced axial strain is related to the displacement by Eq. (36a) ($S_s = 1.93 \times 10^{-6} \mu\text{m}^{-1}$). The solid curves represent least-square fits based on second-order polynomials. The fits are given by Eq. (37a,b). The correlation factor is equal to 0.9999 for both resonators.

is the thickness of the sensor beam and L and a are as indicated in the insert of Fig. 16. The total applied displacement is composed of an offset δ_0 and the micrometer-induced displacement δ : $\delta_t = \delta_0 + \delta$. The offset is caused by the weight of the load bar and by making contact between the micrometer and the load bar. The offset causes shifts in the resonance frequency from 329.375 to 363.763 kHz and from 166.500 to 196.950 kHz for the 210 and 310 μm long beams, respectively. From the frequency measured prior to placing the upper stamp, the residual strain ϵ_0 can be computed, resulting in 46.9 and 44.7 ppm for the 210 and 310 μm long beams, respectively. The calculation is based on Eq. (21), using the value of the plate modulus given by Eq. (35a), and further, $\rho = 2332$ kg/m³ and $\nu = 0.3$. A possible explanation of the distinction in values of the residual strain given by Eq. (35b) and the ones computed above is the fact that the wafer had to be cleaved into strips for doing the strain measurements. Since the samples consist of different materials, it is not unlikely that a new equilibrium situation will occur, which is accompanied by a redistribution of strain.

The solid lines in Fig. 16 represent least-square fits based on second-order polynomials. The fits are given by:

$$f_{\text{fit}}^2 = \begin{cases} 131550 + 1218.24 \delta + 0.66336 \delta^2 & (37a) \\ \text{for the 210 } \mu\text{m long beam} \\ 37562.9 + 518.934 \delta + 0.18111 \delta^2 & (37b) \\ \text{for the 310 } \mu\text{m long beam} \end{cases}$$

where f_{fit} is in kHz and δ in μm . The contributions of the quadratic term relative to the linear term evaluated at full load (i.e., $\delta = 200$ μm), are approximately 11 and 7% for the 210 and 310 μm long beams, respectively. The observed *quadratic* behaviour was not expected according to Eq. (21). The latter equation combined with Eq. (36a) predicts a *linear* relationship between the frequency squared and the applied displacement:

$$\frac{f_1^2}{f_0^2} \approx \left[1 + \gamma_1 (\epsilon_0 + S_s \delta_0) (1 - \nu^2) \left(\frac{L}{h} \right)^2 \right] + \gamma_1 S_s (1 - \nu^2) \left(\frac{L}{h} \right)^2 \delta \quad (38)$$

where ϵ_0 denotes the residual strain and f_0 denotes the resonance frequency in the absence of an external axial load.

From Eqs. (35a), (36) and (38), the measured frequencies and the calculated values of the residual strain, the offset displacement δ_0 can be calculated, resulting in approximately 27 μm for both beam lengths ($S_s = 1.93 \times 10^{-6} \mu\text{m}^{-1}$). Also the coefficient of the linear term in Eq. (37a,b) can be calculated, resulting in 885 and 406 kHz² μm^{-1} for the 210 and 310 μm long beams, respectively. This implies a deviation from the measured value as indicated by Eq. (37) of -27 and -22% for the 210 and 310 μm long beams, respectively. The gauge factor $G_e = (1/f_s)(df_s/d\epsilon)$ evaluated at the operating point defined by $\delta = 0$ can be calculated, resulting in 1730 and 2729 for the 210 and 310 μm long beams, respectively. These calculated values deviate by -28 and -24% from the measured values (i.e., 2400 and 3600) determined from the linear coefficient in Eq. (37a,b) for the 210 and 310 μm long beams, respectively.

The model can be improved by extending the right-hand side of Eq. (36a) with an empirical quadratic term $\theta_1 \delta_t^2$ in which the coefficient θ_1 in general depends on the dimensional parameters. This will lead to a modified expression for the linear coefficient in Eq. (38), leading to more accurate predictions.

A possible explanation for having to add a quadratic term in Eq. (38) is friction. Because the ridges of the stamps are very sharp, this may lead to a rather 'intimate' contact between the bars and the sensor beam. As a result, upon application of a displacement to the structure, the sensor beam will not only bend, but will also experience an axial force leading to enhanced sensitivity. This effect will be more pronounced for large displacements, since higher contact forces between the stamps and the carrier beam then occur, resulting in more friction. To check whether this effect is indeed of importance, the ridges can be made blunter or could resemble dough rolling pins.

4.7. Temperature dependence

In order to measure the dependence of the resonance frequency on temperature, the wafer was placed on a Peltier element. Electric contact to the resonators was made using probes. The results are shown in Fig. 17 for four different beam lengths and a temperature range 10–70 °C. The temperature measurements gave the following temperature coefficients: -135 , -202 , -380 and -394 ppm °C $^{-1}$ for the 210, 310, 410 and 510 μ m long beams, respectively. This turns out to be much greater than the intrinsic coefficient, which is of the order of -40 ppm °C $^{-1}$ [14]. Possible explanations for this discrepancy are found in thermally induced stresses due to mismatches in the thermal expansion coefficients of the different materials (silicon, polysilicon, silicon nitride, aluminium) used. Since the longer beams have a higher gauge factor, this would also explain the increase of the temperature coefficient with increasing beam length. Improvements in terms of a lowering of differential thermal effects can be achieved if the chips are isolated from the mount, e.g., by having the sensor chips hanging at their bonding wires, and/or by removing the aluminium layer from the backside of the wafer (or of the individual chips).

5. Conclusions

The modelling and experimental results of electrostatically driven vacuum-encapsulated polysilicon resonators have been presented. Electrostatic excitation and detection was used as the driving and detection mechanism. Emphasis was placed on a description of resonators that are operated in a one-port configuration. The effective residual strain and the plate modulus of the polysilicon layer can be obtained from the resonance

frequencies measured on microbridges of varying beam length, yielding approximately 36.8 ppm (tensile) and 166 GPa, respectively. The theory as described in this paper is in close agreement with the experiments and as such provides a framework for optimizing the resonator performance.

In a narrow frequency regime around the fundamental mode, the resonator electromechanical behaviour is accurately modelled by an electric network consisting of a capacitor in parallel with an RLC series branch. The series branch represents the mechanical behaviour, whereas the capacitor represents a true electrical capacitance. The dependence of the circuit components on the d.c. polarization voltage is modelled and was confirmed by experiments. The equivalent circuit provides an aid in the analysis and design of the one-port resonator. For such a circuit, two characteristic resonance frequencies can be defined, one associated with the parallel resonance and the other with the series resonance. The series resonance frequency is considered to be the more suitable characteristic frequency since it is not affected by parallel parasitic loads. The theoretical model accounts for the influence of partially overlapping electrodes. This allows optimization of the geometrical design of the electrodes so as to maximize the capacitance ratio and thus the coupling factor and the figure of merit. The hard spring effect or amplitude stiffening leads to unwanted shifts of the resonance frequency. This effect can be kept small by choosing low d.c. polarization voltages and a.c. drive voltages, and further by making the mechanical quality factor not excessively high and introducing a higher residual strain.

Gauge factors indicating the sensitivity of the resonance frequency to axially applied strain were measured using a micrometer-driven four-point beam-deflection jig. Based upon a linear relationship between the applied displacement and the induced strain, gauge factors close to 2400 and 3600 were estimated for polysilicon beams 1.5 μ m thick and 210 and 310 μ m long, respectively. The temperature sensitivity turned out to be greater than the presumed intrinsic dependence of -40 ppm °C $^{-1}$ and is attributed to differential thermal expansion.

Summarizing, it can be said that resonators of this type are promising candidates for applications as resonant strain gauges to replace the conventional (silicon) piezoresistors. It is expected that this will lead to sensors with improved performance. In this context, the following recommendations can be made: the oscillator circuitry should be designed to excite the series mode; external series and parallel loads must be kept as small as possible; the d.c. polarization and a.c. drive voltages must be stabilized; a compromise must be sought between the maximum acceptable level of amplitude stiffening and signal-to-noise ratio on the one hand and

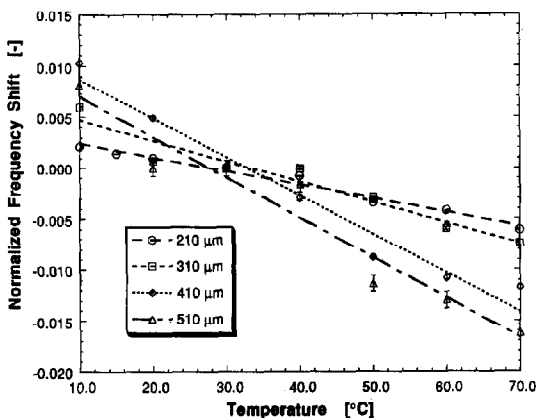


Fig. 17. Normalized resonance frequency shifts vs. temperature for all four beam lengths. The frequency shift is normalized to the resonance frequency at 30 °C.

the achievable resolution of the sensing device on the other hand; to achieve better temperature characteristics, compensation techniques such as a dual or differential design should be employed and/or the use of materials other than (poly)silicon must be avoided as much as possible. In order to verify their application in high-performance sensing applications, the resonators have to be refined and the short-term (frequency noise) and long-term (aging) frequency stability of the devices should be investigated. It goes without saying that the very important issue of packaging must receive more and more attention.

Acknowledgements

The authors acknowledge Dr Miko Elwenspoek, Professor Dr Jan Fluitman and Professor Dr Theo Popma of the micromechanics group for their interest and support. Further, they thank the staff of the MESA Laboratory of the University of Twente, in particular Arie Kooy for mask fabrication, and Eddy de Ruiter, Tom Aarnink and Gerrit Boom for doing the ion implantations. Also they would like to thank Dick Ekkelkamp for his technical support and Hans Schurer and Iwan Bos for doing most of the measurements. This research is part of the programme of the Dutch Foundation for Fundamental Research on Matter (FOM) and is sponsored by the Dutch Technology Foundation (STW).

References

- [1] J.D. Lewis, Pressure sensing: a practical primer, *InTech (USA)*, 35 (1988) 44–47.
- [2] S. Bernhardt, Intelligente Druckaufnehmer auf Resonator-Basis für Präzisionsmessungen, *Elektronik Entwicklung*, 4 (1988) 14–15.
- [3] K. Petersen, F. Pourahmadi, J. Brown, P. Parsons, M. Skinner and J. Tudor, Resonant beam pressure sensor fabricated with silicon fusion bonding, *Proc. 6th Int. Conf. Solid-State Sensors and Actuators (Transducers '91)*, San Francisco, CA, USA, June 24–28, 1991, pp. 664–667.
- [4] J.D. Zook, D.W. Burns, H. Guckel, J.J. Sniegowski, R.L. Engelstad and Z. Feng, Characteristics of polysilicon resonant microbeams, *Sensors and Actuators A*, 35 (1992) 51–59.
- [5] P. Parsons, A. Glendinning and D. Angelidis, Resonant sensors for high accuracy pressure measurement using silicon technology, *IEEE AES Magazine*, 7 (1992) 45–48.
- [6] T. Saigusa, H. Kuwayama, S. Gotoh, M. Yamagata, DPharp series electronic differential pressure transmitters, *Yokagawa Tech. Report English Edn.*, No. 15 (1992) 103–115.
- [7] K. Ikeda, H. Kuwayama, T. Kobayashi, T. Watanabe, T. Nishikawa and T. Yoshida, Silicon pressure sensor with resonant strain gauge built into diaphragm, *Proc. 7th Sensor Symp., Tokyo, Japan*, 1988, pp. 55–58.
- [8] K. Ikeda, H. Kuwayama, T. Kobayashi, T. Watanabe, T. Nishikawa and T. Yoshida, Three dimensional micromachining of silicon resonant strain gauge, *Proc. 7th Sensor Symp., Tokyo, Japan*, 1988, pp. 193–196.
- [9] J.J. Sniegowski, H. Guckel and T.R. Christenson, Performance characteristics of second generation polysilicon resonating beam force transducers, *Proc. IEEE Solid-State Sensors and Actuators Workshop, Hilton Head Island, SC, USA, June 4–7, 1990*, pp. 9–12.
- [10] H. Guckel, C. Rypstat, M. Nesnidal, J.D. Zook, D.W. Burns and D.K. Arch, Polysilicon resonant microbeam technology for high performance sensor applications, *Proc. IEEE Solid-State Sensors and Actuators Workshop, Hilton Head Island, SC, USA, June 22–25, 1992*, pp. 153–156.
- [11] H.A.C. Tilmans, M. Elwenspoek and J.H.J. Fluitman, Micro resonant force gauges, *Sensors and Actuators A*, 30 (1992) 35–53.
- [12] H.A.C. Tilmans, Micromechanical sensors using encapsulated built-in resonant strain gauges, *Ph.D. dissertation*, Faculty of Electrical Engineering, University of Twente, 1993.
- [13] H.A.C. Tilmans, R. Legtenberg, H. Schurer, D.J. Untema, M. Elwenspoek and J.H.J. Fluitman, (Electro)mechanical characteristics of electrostatically driven vacuum encapsulated polysilicon resonators, *IEEE Trans. Ultrasonics, Ferroelectr. Freq. Control*, UFFC-41 (1) (1994) 4–6.
- [14] H.C. Nathanson, W.E. Newell, R.A. Wickstrom and J.R. Davis, Jr., The resonant gate transistor, *IEEE Trans. Electron Devices*, ED-14 (1967) 117–133.
- [15] R.T. Howe and R.S. Muller, Resonant-microbridge vapor sensor, *IEEE Trans. Electron Devices*, ED-33 (1986) 499–506.
- [16] M.W. Putty, S.C. Chang, R.T. Howe, A.L. Robinson and K.D. Wise, One-port active polysilicon resonant microstructures, *Proc. IEEE Micro Electro Mechanical Systems, Salt Lake City, UT, USA, Feb. 20–22, 1989*, pp. 60–65.
- [17] C. Linder, E. Zimmerman and N.F. de Rooij, Capacitive polysilicon resonator with MOS detection circuit, *Sensors and Actuators A*, 25–27 (1991) 591–595.
- [18] H.A.C. Tilmans, D.J. Untema and J.H.J. Fluitman, Single element excitation and detection of (micro-)mechanical resonators, *Proc. 6th Int. Conf. Solid-State Sensors and Actuators (Transducers '91)*, San Francisco, CA, USA, June 24–28, 1991, pp. 533–537.
- [19] D.J. Untema and H.A.C. Tilmans, Static and dynamic aspects of an air gap capacitor, *Sensors and Actuators A*, 35 (1992) 121–128.
- [20] R. Legtenberg and H.A.C. Tilmans, Electrostatically driven vacuum encapsulated polysilicon resonators. Part I: design and fabrication, *Sensors and Actuators A*, 45 (1994) 57–66.
- [21] I.H. Shames and C.L. Dym, *Energy Methods and Finite Element Methods in Structural Mechanics*, McGraw-Hill, New York, 1985, Chs. 3 and 7.
- [22] L. Meirovitch, *Elements of Vibration Analysis*, McGraw-Hill, New York, 1975, Chs. 1 and 5.
- [23] J.G. Easley, Nonlinear vibration of beams and rectangular plates, *J. Appl. Math. Phys.*, 15 (1964) 167–175.
- [24] K. Ikeda, H. Kuwayama, T. Kobayashi, T. Watanabe, T. Nishikawa, T. Yoshida and K. Harada, Study of nonlinear vibration of silicon resonant beam strain gauge, *Proc. 8th Sensor Symp., Tokyo, Japan*, 1989, pp. 21–24.
- [25] M. Andrews, I. Harris and G. Turner, A comparison of squeeze-film theory with measurements on a microstructure, *Sensors and Actuators A*, 36 (1993) 79–87.
- [26] L.M. Zhang, D. Uttamchandani, B. Culshaw and P. Dobson, Measurement of Young's modulus and internal stress micro-resonators using a resonant frequency technique, *Meas. Sci. Technol.*, 1 (1990) 1343–1346.
- [27] R.L. Mullen, M. Mehregany, M.P. Omar and W.H. Ko, Theoretical modeling of boundary conditions in microfabricated beams, *Proc. IEEE Micro Electro Mechanical Systems, Nara, Japan, 30 Jan.–2 Feb., 1991*, pp. 154–159.

- [28] S. Bouwstra, E. de Weerd and M. Elwenspoek, In situ phosphorus-doped polysilicon for excitation and detection of micro-mechanical resonators, *Sensors and Actuators A*, 24 (1990) 227–235.

Biographies

Harrie Tilmans was born on November 14, 1957 in Ensloo, The Netherlands. He received his M.Sc. degree in electrical engineering from the University of Twente, Enschede, The Netherlands, in May 1984. In June 1984 he became a temporary researcher at the University of Twente, where he worked on the development of a resonating force sensor. In April 1985 he joined the Faculty of Electrical and Computer Engineering of Boston University, Boston, MA, USA, as a visiting instructor. In August 1986 he became a research assistant at the Wisconsin Center for Applied Microelectronics at the University of Wisconsin, Madison, WI, USA, where he worked on the development of a CMOS process and on the development of polysilicon micro-mechanical resonators. In August 1988 he returned to The Netherlands where he joined the MESA Research Institute of the University of Twente as a research associate to work on 'micromechanical sensors using

encapsulated built-in resonant strain gauges'. He received his Ph.D. degree on this topic in January 1993. From August 1989 till January 1990 he was on leave from the university at the Sensors Group of the Controls Research Department of Johnson Controls Inc., Milwaukee, WI, USA, working on a low-range differential pressure sensor. From September 1, 1992 till August 1, 1993 he was employed by FOM (Foundation for Fundamental Research on Matter, The Netherlands) in a postdoctorate position within the Micromechanics Group of the MESA Research Institute to work on the characterization of mechanical properties of thin films. He is currently employed by the Catholic University of Leuven in Belgium to continue his work on microsystems technology.

Rob Legtenberg was born on June 21, 1964, in Hengelo, The Netherlands. He received the B.Sc. degree in applied physics, from the Hogere Technische School Enschede, Enschede, The Netherlands, in June 1985. After fulfilling his military service, he joined the MicroMechanical Research Group at the University of Twente as a process engineer in September 1986. Since April 1992 he has been preparing for his Ph.D., dealing with the development of actuators based on surface micromachining technology.